Received: 16 December 2022 | Revised: 9 May 2023 | Accepted: 10 May 2023

IET Microwaves, Antennas & Propagation

DOI: 10.1049/mia2.12373

ORIGINAL RESEARCH

Ranging and multipath-enhanced device-free localisation with densely-meshed ultra-wideband devices

Christian Gentner | **Martin Schmidhammer**

Institute of Communications and Navigation, German Aerospace Center (DLR), Wessling, Germany

Correspondence
Christian Gentner.
Email: christian.gentner@dlr.de

Abstract

Device-free localisation (DFL) is a prominent example of radio sensing and radio frequency (RF)-based passive localisation. RF-based passive localisation approaches determine the position of a non-cooperative user based on the user's impact on radio propagation. In this regard, DFL systems measure user-induced changes in the properties of the received RF signals. With multipath-enhanced device-free localisation (MDFL), a novel passive localisation approach which is taking the advantage of user-induced fading in the multipath signals, that is, reflected and scattered signals is introduced. In this work, the authors realise an MDFL system using low-cost ultra-wideband (UWB) devices. Specifically, the Qorvo (DecaWave) *DW1000* module is used, for which how to access the channel impulse response is described in detail. Additionally, an overview of the required signal processing for MDFL is provided and a possible sequential Bayesian approach is introduced. Moreover, an efficient ranging scheme based on time-division multiple access (TDMA) and message broadcasting is outlined, which allows the deployment of a large number of interconnected UWB devices. Using an exemplary network of interconnected UWB devices, the localisation performance of both DFL and MDFL for an indoor scenario is evaluated. Thereby, MDFL is shown to clearly outperform DFL in terms of robustness and accuracy. Furthermore, a TDMA-based ranging scheme for active localisation is used, that is, for localising an UWB device carried by the user, allowing for a direct comparison between active and passive localisation. Achieving a sub-decimetre accuracy, the active localisation outperforms both DFL and MDFL, and thus, shows the possibility of using an active localisation device to initialize MDFL.

KEYWORDS

Bayes methods, global positioning system, Kalman filters, radio networks, ultra wideband technology, wireless sensor networks

1 | INTRODUCTION

Indoor localisation has received at lot of attention in recent years and is expected to become even more important in the future. Whereas for outdoor global navigation satellite systems (GNSSs) are commonly used for localisation, the localisation accuracy of GNSSs in indoor scenarios is drastically reduced or even impossible. In these situations, the received GNSS signals might be blocked, degraded by multipath effects or received with low power [1]. To enhance the localisation performance indoors, different methods and sensor systems can provide position information rather than relying on GNSSs. Most of the indoor localisation systems are active radio frequency (RF)-based localisation systems, which require the user to carry a localisation device like a smartphone. Alternatively, passive localisation systems estimate presence and location of a non-equipped user by measuring the user's impact on the propagation of RF signals [2, 3]. A prominent example of an RF-based sensing technology is device-free localisation (DFL) [2]. In DFL, static transceiving nodes are exchanging RF

Christian Gentner and Martin Schmidhammer have equally contributed as co-first authors.

signals between each other. The presence and location of a non-equipped user can be inferred, by measuring the received power between transceiving nodes along the line-of-sight (LoS) path. The DFL system directly relates these received power measurements to the user location [2, 4–7], thereby, the localisation accuracy of such DFL systems improves with the number of network nodes [6, 7].

In refs. [3, 7, 8], we introduced a novel algorithm which extends and improves the DFL system by using multipath propagation. We consider the propagation paths of multipath components (MPCs) as additional network links and showed, that user-induced fading can be also observed in the received power of these propagation paths. For the same amount of network nodes, multipath-enhanced device-free localisation (MDFL) is shown to improve the localisation performance compared to DFL and helps to reduce infrastructural requirements.

In ref. [9], we have shown how to realise an MDFL system using low-cost ultra-wideband (UWB) devices. Specifically, we used modules based on the Qorvo (DecaWave) *DW1000* module [10] and a *Raspberry Pi 4 Model B*[1]. Basically, an MDFL system relies on the processing of the channel impulse response (CIR) between the different modules. We have therefore described in detail how to access the CIR of the *DW1000* module and how to estimate and process required signal parameters. For synchronisation, we applied a double-sided two-way ranging (DS-TWR) procedure for determining absolute time information between the individual UWB devices.

In this work, we apply the MDFL system to a densely-meshed network of UWB devices. Following ref. [11], we apply a time-division multiple access (TDMA) scheme, allowing a large number of UWB devices to successively broadcast sensing messages. We show how to determine the absolute time information between the individual UWB devices similar to the DS-TWR method. After introducing a possible Bayesian MDFL solution, we finally examine the experimental setup using an example trajectory in an indoor scenario. We compare the MDFL to the DFL solution. Thereby, MDFL is shown to clearly outperform DFL in terms of robustness and accuracy. Furthermore, we use the TDMA-based ranging scheme for active localisation implemented using an extended Kalman filter (EKF). Here, a user carried an UWB device which allowed a direct comparison between active and passive localisation.

2 | SYSTEM SETUP AND SIGNAL PROCESSING

In this section, we provide the signal processing for measuring user-induced fading to MPCs required for MDFL. In particular, we introduce the signal model and describe how to access the CIR of DWM1000 UWB modules. Subsequently, we detail the principles of an efficient ranging scheme that enables the deployment of a large number of interconnected UWB devices.

2.1 | Signal model

Let's consider a meshed network with N_C transceiving nodes $C_1, \ldots C_{N_C}$ with known locations at $\boldsymbol{r}_{C_i}$, $i \in \{1, \ldots, N_C\}$. The network link configuration is then determined by the index set $\mathcal{P}$, where link l is determined by the ith transmitting and the jth receiving node, that is, $(i,j) \in \mathcal{P}$ [3].

For a network link l, the received signal, that is, the CIR, is modelled as a superposition of scaled and delayed replica of a known transmit signal $s_l(t)$ due to reflections and scattering [12]. Ideally, the transmit signal would be a Dirac impulse. However, due to limited bandwidth and hardware imperfections, we had to explicitly determine the reference signal in an anechoic chamber. Parts of the determined reference signal are illustrated in Figure 1. Eventually, the modelled received signal comprises the LoS component and a finite number of N_l MPCs, which can be expressed as

$$y_l(t) = \sum_{n=1}^{N_l} \alpha_{l,n}(t) s_l\left(t - \tau_{l,n}\right) + n_l(t), \tag{1}$$

with time-variant, complex amplitude $\alpha_{l,n}(t)$ and static propagation delay $\tau_{l,n}$ of the nth signal component. The circular symmetric normal distributed noise is denoted as $n_l(t)$ with variance $\sigma^2_{y_l}$.

Since MDFL uses variations in the received power of signal components for localisation, it is essential to know the corresponding physical propagation paths. While inherently given for the LoS by the respective locations of the transmitting and receiving nodes, we need to model the propagation paths of MPCs. As shown in ref. [3], we can use virtual nodes, that is, virtual transmitters (VTs) and virtual receivers (VRs) as mirrored positions of the respective physical nodes, to describe the propagation paths. Thereby, the intersection points between paths of related nodes correspond to the physical reflection points, which finally allow to geometrically reconstruct the propagation paths, cf. [1, 3].

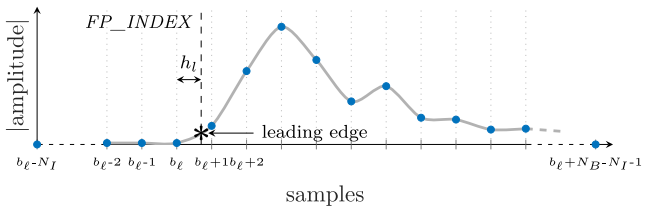

FIGURE 1 Sampled channel impulse response (CIR) of reference signal in the *Accumulator CIR memory* of the Qorvo (DecaWave) *DW1000* module. The blue dots indicate sampling points and *FP_INDEX* shows the detected leading edge of the *DWM1000* module.

[1]Please note, instead of the *Raspberry Pi 4 Model B*, also other microcontrollers can be used.

2.2 | Channel impulse response of DW1000 UWB modules

In this work, we demonstrate the applicability of MDFL using low-cost UWB devices. Therefore, we utilise modules based on the *Qorvo (DecaWave) DW1000* transceiving module [10]. In our case, we use a breakoutboard equipped with the *DWM1000* module[2] and connect it to the general-purpose input/output (GPIO) of a *Raspberry Pi 4 Model B*, see Figure 2. The *Raspberry Pi 4 Model B* is used as the processing unit, which is controlling the *DW1000* transceiving module by serial peripheral interface (SPI). Additionally, the *Raspberry Pi 4 Model B* offers the possibility to connect storage devices and provides a variety of communication interfaces such as Ethernet, wireless local area network (WLAN), and Bluetooth. In the following, we refer to this hardware setup, that is, a *Raspberry Pi 4 Model B* together with a *DWM1000* module, as a transceiving node.

The *DW1000* module time stamps transmitted and received UWB signals, which can be accessed by a processing unit. Based on these time stamps, ranges between different transceiving nodes can be estimated, see Section 2.3. For time stamping received signals, the *DW1000* module detects the leading edge of the corresponding CIR. For detailed information about the leading edge detection algorithm see [10]. Additional to the times stamps, the *DW1000* module amongst others stores the sampled CIR in an *Accumulator CIR memory*. The *Accumulator CIR memory* contains the complex 16 bit raw samples of the CIR, sampled with a frequency of $f_s = 1$ GHz. The detected leading edge is expressed in subsamples, denoted as h_f, and stored in the *FP_INDEX* field of the *Receive Time Stamp* register. Therewith, the value of *FP_INDEX* indicates the exact position of the leading edge of the CIR in the *Accumulator CIR memory*, as shown in Figure 1. The 16 bits of *FP_INDEX* are divided into two parts. First, the 10 most significant bits represent the integer sample number $b_\ell = \lfloor h_f/64 \rfloor$, that is, the sample prior to the leading edge, cf. Figure 1. Second, the six least significant bits represent the fractional part $h_\ell = h_f - \lfloor h_f/64 \rfloor$, that is, the interval between b_ℓ and the leading edge as illustrated in Figure 1.

For further processing, we extract N_B samples from the *Accumulator CIR memory*. That means, we download the samples $B = \{B_1, \ldots, B_{N_B}\}$ with the sample indexes $w \in \{b_\ell - N_I, \ldots, b_\ell, \ldots, b_\ell + N_B - N_I - 1\}$. To assure to access all information of the CIR, we download N_I samples before the detected leading edge, which is also shown in Figure 1.

Until now, the CIR has no time reference. In order to obtain a time reference of the CIR, that is, to obtain the CIR as a function of time, the corresponding transceiving nodes need to be synchronised, see for example, [11, 13–15]. Since the signal propagation time is proportional to the propagation distance, time synchronisation can achieved by estimating the distance $\widehat{d}_{a,b}$ between two transceiving nodes C_a and C_b. Thus, the CIR at C_a can be described as a function of the estimated distance $\widehat{d}_{a,b}$. Note that a corresponding ranging scheme is explained in detail in Section 2.3. Each sample index w is related to a distance value $\widehat{d}_{s,w} = \widehat{d}_{a,b} - h_\ell\lambda_s + (w - b_\ell)\lambda_s$, where $\lambda_s = c/f_s$ is the sample spacing and c is the speed of light. Finally, we can express the CIR as a function of time using the time values $\widehat{\tau}_{s,w} = \widehat{d}_{s,w}/c$.

2.3 | Efficient ranging protocol for UWB networks

A promising method for accurate distance estimation between two nodes, is provided by DS-TWR, which allows to achieve distance estimation without a common clock synchronisation and is able to compensate for linear clock drifts of the nodes, cf. [15]. Figure 3 illustrates the DS-TWR method, where transceiving node C_a is initiating the DS-TWR method with C_b. Based on the transmitting time stamps $T_1^{(a)}, T_1^{(b)}, T_2^{(a)}$ and receiving time stamps $R_1^{(b|a)}, R_1^{(a|b)}, R_2^{(b|a)}$, cf. Section 2.2, we can calculate the round-trip times between transceiving nodes

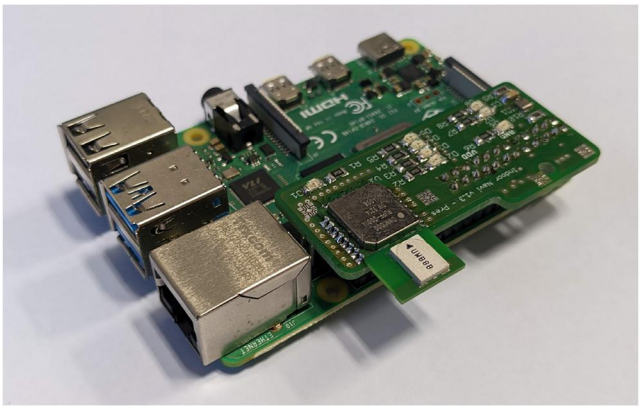

FIGURE 2 Transceiving node including processing unit: *DWM1000* module connected to a *Raspberry Pi 4 Model B* by a breakout board.

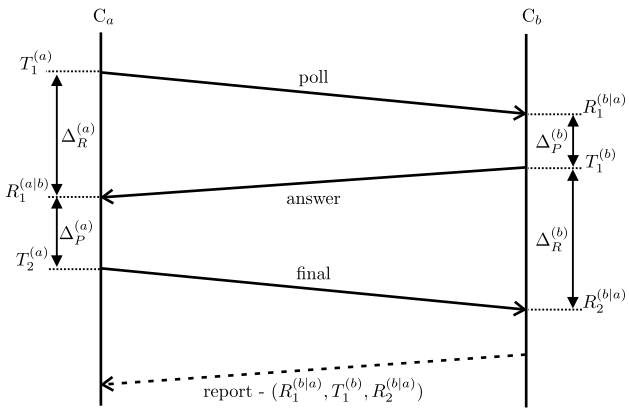

FIGURE 3 Illustration of the double-sided two-way ranging protocol to estimate the distance between two transceiving nodes, that is, transceiving nodes C_a and C_b.

[2]The *DWM1000* module is based on the *DW1000* UWB transceiver IC and integrates antenna, all RF circuitry, power management and clock circuitry in one module.

C_a and C_b as $\Delta_R^{(a)} = R_1^{(a|b)} - T_1^{(a)}$ and $\Delta_R^{(b)} = R_2^{(b|a)} - T_1^{(b)}$, and the processing times $\Delta_P^{(a)} = T_2^{(a)} - R_1^{(a|b)}$ and $\Delta_P^{(b)} = T_1^{(b)} - R_1^{(b|a)}$. Following ref. [15], the distance $d_{a,b}$ is then calculated by

$$\widehat{d}_{a,b} = c \times \frac{\left(\Delta_R^{(a)} \cdot \Delta_R^{(b)}\right) - \left(\Delta_P^{(a)} \cdot \Delta_P^{(b)}\right)}{\Delta_R^{(a)} + \Delta_P^{(a)} + \Delta_R^{(b)} + \Delta_P^{(b)}}. \tag{2}$$

Please note, to calculate the distance $\widehat{d}_{a,b}$ at the transceiving node C_a, the time stamps $R_1^{(b|a)}, T_1^{(b)}, R_2^{(b|a)}$ of C_b are forwarded from C_b to C_a using a dedicated report message.

In case of a fully-meshed network with N_C transceiving nodes, the ranging procedure has to be performed for a total of $N_C(N_C - 1)/2$ links, which scales quadratically with the number of transceiving nodes. Thus, an increasing number of transceiving nodes N_C leads to strongly increasing update times, since the ranging procedure is performed sequentially, and to an immense load on the radio channel due to the required message exchange. Therefore, in ref. [11] we proposed a novel approach for estimating the distance between N_C nodes. The approach uses a TDMA scheme which consists of slots and frames. Each transceiving node broadcasts/transmits a message at a dedicated time slot. Additionally, each transceiver listens to the channel and records all receive times of the neighbouring transceiver.

Figure 4 illustrates the proposed approach of ref. [11]. The figure shows an example with four different transceiving nodes: C_1, C_2, C_3, and C_{N_C}. The rectangular boxes indicate the different frame-identification numberss (IDs), with frame-ID k and frame-ID $k+1$. In frame-ID k, C_1 transmits a message at time $T_k^{(1)}$, all other transceiving nodes a' with $a' \in \{2, 3, N_C\}$ are recording the receiving time stamps $R_k^{(a'|1)}$. Thereafter, C_{N_1} transmits a message at $T_k^{(2)}$, and all other transceiving nodes a'', with $a'' \in \{1, 3, N_C\}$, are recording the receiving time stamps $R_k^{(a''|2)}$. This procedure is done for the whole TDMA frame with frame-ID k, that all nodes are transmitting. In the next frame, frame-ID $k+1$, the transmission and reception is done equivalently.

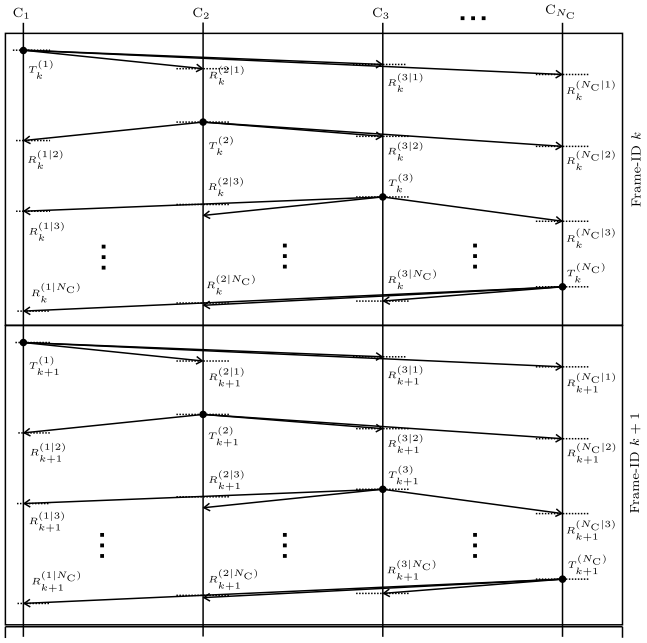

FIGURE 4 Proposed time-division multiple access double-sided two-way ranging scheme to estimate distances between different nodes.

By knowing the receiving and transmitting time stamps, the distance $\widehat{d}_{a,b}$ between C_a and C_b, can be calculated using Equation (2) with

$$\Delta_R^{(a)} = R_k^{(a|b)} - T_k^{(a)} \tag{3}$$

$$\Delta_R^{(b)} = R_{k+1}^{(b|a)} - T_k^{(b)} \tag{4}$$

$$\Delta_P^{(a)} = T_{k+1}^{(a)} - R_k^{(a|b)} \tag{5}$$

$$\Delta_P^{(b)} = T_k^{(b)} - R_k^{(b|a)} \tag{6}$$

for $b > a$ and

$$\Delta_R^{(a)} = R_{k+1}^{(a|b)} - T_k^{(a)} \tag{7}$$

$$\Delta_R^{(b)} = R_{k+1}^{(b|a)} - T_{k+1}^{(b)} \tag{8}$$

$$\Delta_P^{(a)} = T_{k+1}^{(a)} - R_{k+1}^{(a|b)} \tag{9}$$

$$\Delta_P^{(b)} = T_{k+1}^{(b)} - R_k^{(b|a)}, \tag{10}$$

for $a > b$. The individual time stamps can be shared by a cloud service, as in ref. [11], or distributed as payload using the UWB ranging messages. Note that for the latter, the number of transceiving nodes could be limited by the data throughput of the UWB standard. Furthermore, note that the proposed TDMA ranging protocol can mitigate the clock drifts of the different nodes as long as the clocks can be assumed to drift linearly. In order to ensure this assumption, the frame duration has to be chosen as low as possible.

3 | MULTIPATH-ENHANCED DEVICE-FREE LOCALISATION

The following section outlines the principles of MDFL as a radio sensing approach. First, we describe how user-induced fading on individual MPCs is measured from the extracted CIRs (cf. Section 2), including both system initialisation and online parameter estimation. Then, based on a measurement model that relates fading on MPCs to a user's location, we present a Bayesian MDFL realisation for user localisation and tracking.

3.1 | System initialisation

Initially, we need to determine the propagation effects of the static environment for each network link. Therefore, we observe the channel of each network link over an initialisation period, during which the environment should be ideally devoid of any user. We then determine the amplitude and delay values of all separable MPCs for each captured signal sample, that is, CIR, using maximum likelihood estimation, for example, the space-alternating generalised expectation-maximisation (SAGE) algorithm [16]. A subsequent averaging of the parameter estimates results in sets of mean amplitude and mean delay for each network link.

Next, for MDFL we need to determine the physical propagation paths that correspond to these sets of parameter estimates. A possible solution is described in ref. [3] using data association. This involves first computing sets of expected propagation delays, assuming prior information about the surrounding environment, for example, as in this work, by a floor plan. And second, matching the sets of estimated and expected propagation delays following optimal subpattern assignment [17]. Therewith, we obtain N_l assigned delay estimates, that is, MPCs, for link l, where each assigned MPC corresponds to a known physical propagation path. Particularly, we get the assigned set of mean amplitude $\{\overline{\alpha}_{l,q}\}_{q=1}^{\check{N}_l}$ and of mean delay $\{\overline{\tau}_{l,q}\}_{q=1}^{\check{N}_l}$. Based on the set of mean amplitude we can calculate the power of the MPCs for the idle channel serving as reference to determine user induced power changes. Thus, in logarithmic domain, the power level of the qth signal component of link l is

$$\overline{\gamma}_{l,q} = 20\log_{10}\left|\overline{\alpha}_{l,q}\right|. \tag{11}$$

An example is provided in Figure 6, which shows the CIR that corresponds to the link between $\boldsymbol{r}_{C_1}$ and $\boldsymbol{r}_{C_2}$ of the setup shown in Figure 5. Additionally, Figure 6 shows $\check{N}_l = 4$ assigned delay estimates, where $q = 1$ refers to the LoS component. The corresponding physical propagation paths are highlighted in Figure 5.

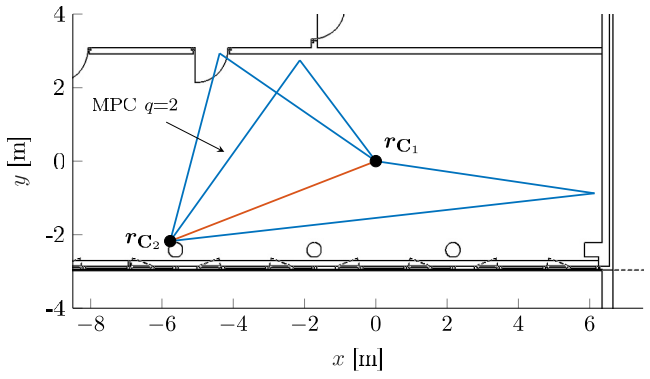

FIGURE 5 Measurement example, showing two transceiving nodes C_1 and C_2 at the locations $\boldsymbol{r}_{C_1}$ and $\boldsymbol{r}_{C_2}$. The multipath propagation is explicitly highlighted, that is, the physical propagation paths of line-of-sight and multipath components are indicated in red and blue.

3.2 | Online parameter estimation

After initialisation, we can now measure the changes of the received power of all considered signal components by determining the amplitude values. Therefore, we calculate the amplitude of the qth signal component of link l given the mean delay $\overline{\tau}_{l,q}$ as

$$\widehat{\alpha}_{l,q} = \widehat{\alpha}\left(\overline{\tau}_{l,q}\right) = \int_0^{T_p} \left(y_{l,q}^{\mathrm{res}}(t)\right)^* s_l\left(t - \overline{\tau}_{l,q}\right) dt, \tag{12}$$

which equals the projection of the residuum signal $y_{l,q}^{\mathrm{res}}(t)$ onto the unit transmit signal $s_l(t)$ [3, 18]. The residuum signal is thereby calculated by adjusting the received signal for all signal components up to the $(q-1)$th, that is,

$$y_{l,q}^{\mathrm{res}}(t) = y_l(t) - \sum_{q'=1}^{q-1} \widehat{\alpha}_{l,q'} s_l\left(t - \overline{\tau}_{l,q'}\right). \tag{13}$$

With the estimated amplitude, we can then express the measured power in logarithmic domain as

$$\widehat{\gamma}_{l,q} = 20\log_{10}\left|\widehat{\alpha}_{l,q}\right|, \tag{14}$$

and subsequently, by subtracting the reference power in Equation (11) from the measured power in Equation (14), the user-induced power changes as

$$z_{l,q} = \widehat{\gamma}_{l,q} - \overline{\gamma}_{l,q} = 20\log_{10}\left|\frac{\widehat{\alpha}_{l,q}}{\overline{\alpha}_{l,q}}\right|. \tag{15}$$

By stacking the measured power changes in Equation (15) for all signal components of all available links, we can compose the measurement vector $\mathbf{z} \in \mathbb{R}^{N^*}$, with $N^* = \sum_{l=1}^{|\mathcal{P}|} \check{N}_l$ as the overall amount of available signal components for MDFL.

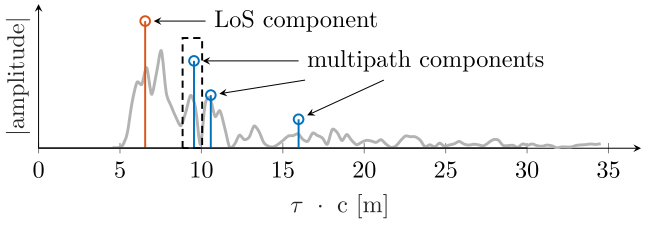

FIGURE 6 Exemplary channel impulse response corresponding to the network link between $\boldsymbol{r}_{C_1}$ and $\boldsymbol{r}_{C_2}$ of Figure 5. Estimated line-of-sight (LoS) component and multipath components (MPCs) are indicated by red and blue stems respectively. MPC $q = 2$ highlighted by dashed rectangle corresponds to the propagation path of the example MPC shown Figure 5.

3.3 | Measurement model

For applying MDFL, we require a model $f(\boldsymbol{r})$ that relates the measured power changes of the signal components to the user location $\boldsymbol{r}$. Following ref. [3], we approximate the user impact on the power of signal components by the empirical exponential model

$$f(\boldsymbol{r}) = \sum_{u=0}^{N_{\tau_{l,q}}} \phi_{l,q} e^{-\xi_{l,q}^{(u)}(\boldsymbol{r})/\kappa_{l,q}}, \tag{16}$$

with $\phi_{l,q}$ and $\kappa_{l,q}$ defining the maximum modelled power change and the spatial decay rate respectively. The excess path length $\xi_{l,q}^{(u)}(\boldsymbol{r})$ of the uth pair of virtual nodes corresponding to delay $\tau_{l,q}$ is calculated by

$$\xi_{l,q}^{(u)}(\boldsymbol{r}) = \|\boldsymbol{r}_{\mathrm{VT}_{l,q}}^{(u)} - \boldsymbol{r}\| + \|\boldsymbol{r}_{\mathrm{VR}_{l,q}}^{(N_{l,q}-u)} - \boldsymbol{r}\| - d_{l,q}, \tag{17}$$

where $\boldsymbol{r}_{\mathrm{VT}_{l,q}}^{(u)}$ and $\boldsymbol{r}_{\mathrm{VR}_{l,q}}^{(N_{\tau_{l,q}}-u)}$ denote the locations of VTs and VRs with $u \in \left\{0, \ldots, N_{\tau_{l,q}}\right\}$ and $d_{l,q}$ refers to the length of the propagation path. Thereby, $N_{\tau_{l,q}}$ provides the order of reflection of the considered signal component. That means for the LoS component $N_{\tau_{l,1}} = 0$, for MPCs due to single-bounce reflection (SBR) $N_{\tau_{l,q}} = 1$, and for higher order reflections $N_{\tau_{l,q}} > 1$. Note for notational convenience the physical transmitting and receiving nodes are referred to as $\boldsymbol{r}_{\mathrm{VT}_{l,q}}^{(0)}$ and $\boldsymbol{r}_{\mathrm{VR}_{l,q}}^{(0)}$. The relation between user location, that is, excess path length, and measured power change is illustrated in Figure 7, showing power change measurements as a function of the excess path length for the example MPC $q = 2$ corresponding to the link between $\boldsymbol{r}_{\mathrm{C}_1}$ and $\boldsymbol{r}_{\mathrm{C}_2}$ of the setup shown in Figure 5. Additionally, Figure 7 also provides the corresponding empirical exponential model with a maximum modelled power change of $\phi = -7.94$ dB and a decay rate of $\kappa = 0.015$ m. It can be clearly seen that the closer the user is to the propagation path, that is, the smaller the excess path length, the greater the measured negative power changes. Note that a negative power change equals an attenuation of the received power. Thus, the strongest attenuation can be observed when the user is located directly on the propagation path, that is, when the excess path length equals zero.

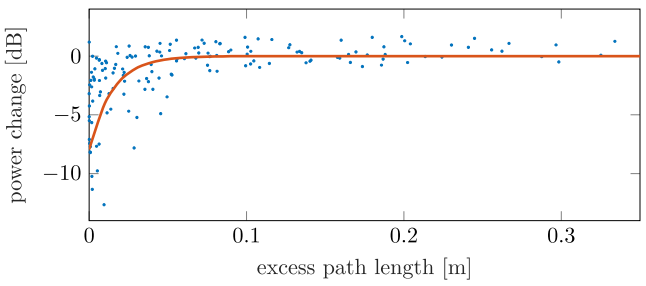

FIGURE 7 Measured power changes of example multipath component $q = 2$ as highlighted in Figures 5 and 6 as a function of excess path length. For illustration purposes, the minimum excess path length is used for the abscissa. The corresponding empirical exponential model is illustrated in red with a maximum modelled power change of $\phi = -7.94$ dB and a decay rate of $\kappa = 0.015$ m, cf. (16).

3.4 | Bayesian MDFL

Finally, we can formulate the localisation problem of MDFL using the state-space representation. That means, first, by a measurement model relating the user state $\mathbf{x}_k = \boldsymbol{r}_k$, that is, the user location at time instant k, to the measured power changes of signal components. That means, we model the measurement vector $\mathbf{z}_k$, cf. Equation (15), using Equation (16) as

$$\mathbf{z}_k = f(\mathbf{x}_k) + \mathbf{w}_k, \tag{18}$$

where $\mathbf{w}_k \, \widetilde{\mathcal{N}}(\mathbf{0}, \mathbf{R})$ denotes Gaussian measurement noise with the diagonal covariance matrix $\mathbf{R} \in \mathbb{R}^{N^* \times N^*}$ [3]. And second, by a transition model describing the spatio-temoral evolution of the user location, given by the state equation

$$\mathbf{x}_k = \mathbf{A}\mathbf{x}_{k-1} + \mathbf{n}_k, \tag{19}$$

where $\mathbf{A}$ represents the transition matrix and $\mathbf{n}_k \, \widetilde{\mathcal{N}}(\mathbf{0}, \mathbf{Q})$ denotes the Gaussian process noise with covariance matrix $\mathbf{Q}$. For the two-dimensional user state $\mathbf{x}_k$, the transition and the covariance matrix of the process noise can be written as

$$\mathbf{A} = \begin{bmatrix} 1 & 0 \\ 0 & 1 \end{bmatrix}, \quad \mathbf{Q} = \sigma_p^2 \begin{bmatrix} \frac{T_g^3}{3} & 0 \\ 0 & \frac{T_g^3}{3} \end{bmatrix}, \tag{20}$$

with T_g as time between two adjacent measurements and σ_p^2 as process noise intensity of physical dimension $[\mathrm{m}^2\mathrm{s}^3]$ [19].

In a Bayesian context, the measurement and transition models can be expressed by the conditional probability density function (PDF) $p(\mathbf{z}_k \mid \mathbf{x}_k)$ and the transition prior distribution $p(\mathbf{x}_k \mid \mathbf{x}_{k-1})$. Thereby, sequential Bayesian estimation aims to determine the PDF of the user state by computing the posterior density $p(\mathbf{x}_k \mid \mathbf{z}_{1:k})$ using general Bayesian update recursion [20]. As shown in ref. [8], a possible Bayesian approach for solving the non-linear system represents the particle filter (PF). The PF approximates the non-Gaussian posterior density of our localisation problem with a discrete density

$$p(\mathbf{x}_k|\mathbf{z}_{1:k}) \approx \sum_{i=1}^{N_s} w_k^i \delta\left(\mathbf{x}_k - \mathbf{x}_k^i\right), \tag{21}$$

where $\delta(\cdot)$ denotes the Dirac delta function and $\mathbf{x}_k^i$ represents the ith particle of the stochastic set of particles $\left\{\mathbf{x}_k^i\right\}_{i=1}^{N_s}$ and

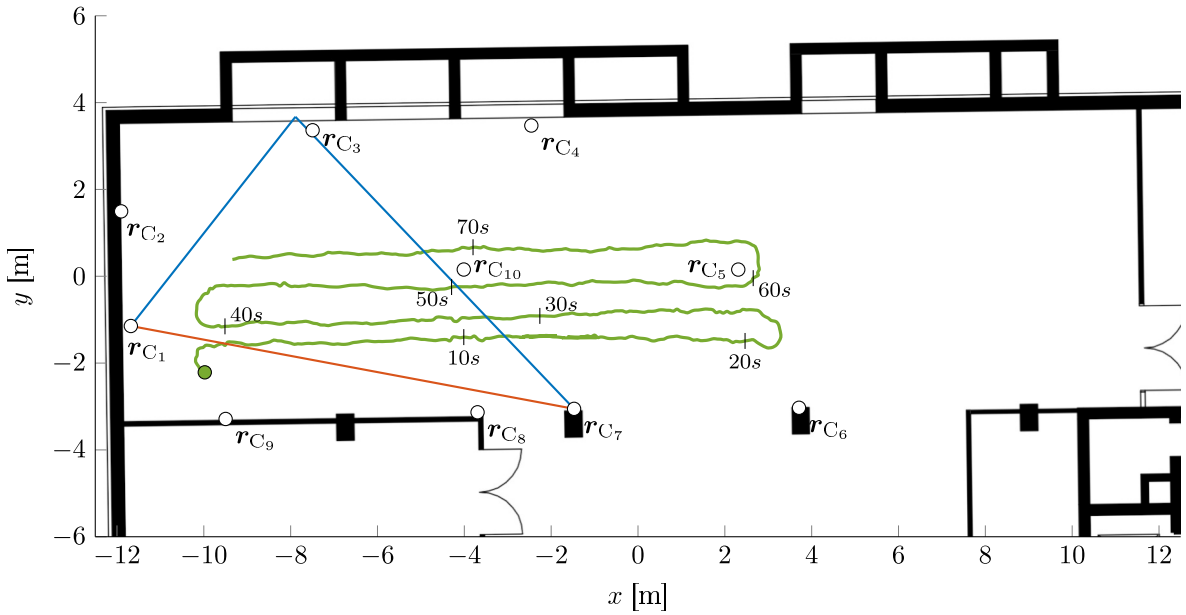

FIGURE 8 Measurement setup including $N_C = 10$ transceiving nodes located at $\boldsymbol{r}_{C_i}$ with $i \in \{1, \ldots, 10\}$ and the ground truth trajectory of a user indicated in green. The starting position of the user trajectory is indicated by a bold green dot. Exemplary propagation paths for the link between network nodes $\boldsymbol{r}_{C_1}$ and $\boldsymbol{r}_{C_7}$ are shown in red for the line-of-sight component and in blue for the multipath component due to reflection from the outer wall.

weight $\{w_k^i\}_{i=1}^{N_s}$. In this work, we apply the generic PF [20] and assume that the particles are drawn from an importance density, which is set equal to the transition prior distribution, simplifying the weight update to

$$w_k^i = \frac{1}{c_k} w_{k-1}^i p\left(\mathbf{z}_k | \mathbf{x}_k^i\right). \tag{22}$$

The normalisation is calculated as $c_k = \sum_{j=1}^{N_s} w_{k-1}^j p\left(\mathbf{z}_k | \mathbf{x}_k^j\right)$ and $p\left(\mathbf{z}_k | \mathbf{x}_k^i\right)$ denotes the likelihood distribution. In order to counteract the problem of degeneracy, we apply resampling [20].

4 | EVALUATION BASED ON MEASUREMENTS

In this section, we evaluate and demonstrate the proposed MDFL algorithm using the proposed UWB measurement setup. The UWB measurement setup is shown in Figure 8 and consists of a meshed network with $N_C = 10$ transceiving nodes $C_1, \ldots, C_{10}$ located at $\boldsymbol{r}_{C_i}$ with $i \in \{1, \ldots, 10\}$, all at the same height of 0.8 m above the ground. The *DW1000* modules are configured to a bandwidth of 500 MHz and a carrier frequency of 3.9 GHz. Further, we consider the trajectory of a user walking for almost 80 s in the measurement area, indicated by the green path in Figure 8. The starting position is shown by the bold green dot. During the measurements, the user was additionally carrying a mobile transceiving node in his hands (texting mode). This transceiving node was also performing the TDMA scheme and hence the distance estimates can also be evaluated for comparison. The ground truth of the static and mobile transceiving nodes was recorded using a Vicon[3] high-precision optical motion capture system consisting of 20 infrared cameras and infrared strobes. This setup can locate objects in the observation area with a distance error of less than 1 cm and is used a ground truth system.

While the user followed the trajectory, we have continuously measured the CIRs of all links. Thereby, the frame rate of the TDMA scheme was approximately 10 Hz, resulting in an update time of $T_g \approx 0.1$ s for each link. Then the power changes of all signal components for each network link are determined as described in Section 3.2. Exemplary, Figure 9 shows the measured power changes over time for the example MPC of the link between transceiving nodes C_1 and C_7, cf. Figure 8. As shown in Figure 8, the user crosses the MPC after 12 s, 32 s, 50 s, and 72 s. This can be also clearly seen in Figure 9, where the power changes substantially when the user crosses the MPC. Further, we can observe a good match between the measured and the modelled power changes, calculated using Equation (16) and the ground truth data.

Figure 10 shows the floor plan of the measurement area with the spanned meshed network: the network consists of $N_C(N_C - 1)/2 = 45$ LoS components, indicated in red, and of 78 MPCs due to first-order reflections, indicated in light grey. We can clearly observe MPCs which were reflected on the outer walls or on the metallic entrance door shown on the right of Figure 10. Additionally, we can see MPCs originated from objects and furniture in the laboratory. Given the measured power changes, we can now compose the measurement vectors

[3] https://www.vicon.com.

for DFL and MDFL as $\mathbf{z}_k^{\mathrm{DFL}} \in \mathbb{R}^{45}$ and $\mathbf{z}_k^{\mathrm{MDFL}} \in \mathbb{R}^{123}$ respectively.

Finally, we apply the PF for localisation. For the PF we use $N_s = 1000$ particles, a process noise intensity of $\sigma_p = 0.5\ \mathrm{m}^2/\mathrm{s}^3$, and assume $\sigma = 1.25$ dB for all elements of the measurement noise covariance matrix. The PF is initialised by randomly distributing the particle states within the measurement area. For obtaining a point estimate from the posterior density of Equation (21), we compute the weighted sum $\widehat{\mathbf{x}}_k = \sum_{i=1}^{N_s} w_k^i \mathbf{x}_k^i$, also known as the minimum mean square error (MMSE) criterion. Based on the point estimate $\widehat{\mathbf{x}}_k$, we can then compute the root mean square error (RMSE) as

$$\mathrm{RMSE}_k = \sqrt{E\left[\|\widehat{\mathbf{x}}_k - \mathbf{x}_k\|^2\right]}, \tag{23}$$

where $\mathbf{x}_k$ refers to the true user location.

As mentioned before, we compare in the following the PF implementation of the DFL and the MDFL to an active localisation algorithm. The active localisation algorithm was implemented using an EKF, which uses the distance estimates obtained from the mobile transceiving node as inputs. Similar to the PF implementation of the DFL and MDFL, the EKF uses the transition and the covariance matrix of the process noise as described in Equation (20). Figure 11 shows the estimated distances and the distance estimation errors as a function of time in seconds between four example transceiving nodes, that is, C_1, C_3, C_8, C_{10}, and the mobile transceiving node. We can observe, that we are able to obtain accurate distance estimates using the TDMA scheme. In some cases the distance error goes up to 2 m, which could be caused by signal blockage of the user.

Accounting for the stochastic nature of PFs, we have evaluated 100 realisations for both DFL and MDFL. Consequently, the RMSE results are determined by averaging over these realisations. The results for the evaluated user trajectory are shown in Figure 13. For MDFL, we can observe an RMSE curve without strong outliers over the entire trajectory. With a mean RMSE of 0.40 m, MDFL clearly outperforms DFL, which achieves a mean RMSE of 2.52 m, cf. Table 1. Comparing the RMSE results of DFL and MDFL in more detail, we would like to point out two observations. First, the decrease of the RMSE during the initial time period: At the starting point, the RMSE is similar for both DFL and MDFL, since the PFs are initialised randomly. However, MDFL converges faster to a solid location solution compared to DFL. That faster convergence can be explained by the network structure shown in Figure 10. Shortly after the starting point, the user moves through the propagation paths of multiple MPCs. The measured power changes for these MPCs allow MDFL to immediately resolve a distinct location solution. DFL, on the other hand, considering LoS components only, relies on very few initial power change measurements. At the starting point, the user impacts the power of the link between nodes C_2 and C_9 only, cf. Figure 10. Second, the robustness of the localisation performance: While for MDFL the localisation performance remains almost stable throughout the scenario, we can observe periods of severely degraded RMSE

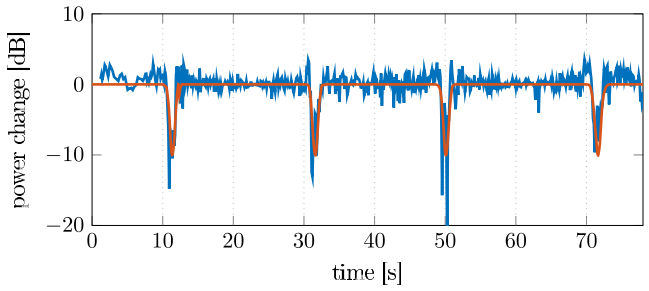

FIGURE 9 Power changes of the example multipath component (MPC) of the link between transceiving nodes C_1 and C_7 shown in Figure 8 over time. The measured power changes correspond to the trajectory shown in Figure 8, where the user crosses the MPC after 12 s, 32 s, 50 s, and 72 s. The corresponding empirical exponential model is illustrated in red.

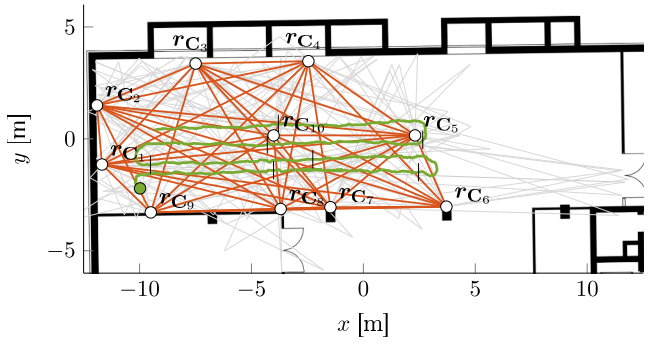

FIGURE 10 Visualisation of the network spanned by the measurement setup including $N_C = 10$ transceiving nodes at $\boldsymbol{r}_{C_i}$ with $i \in \{1, \ldots, 10\}$. Propagation paths of 45 line-of-sight components (fully-meshed network) are indicated in red and of 78 multipath components due to first-order reflections are indicated in light grey.

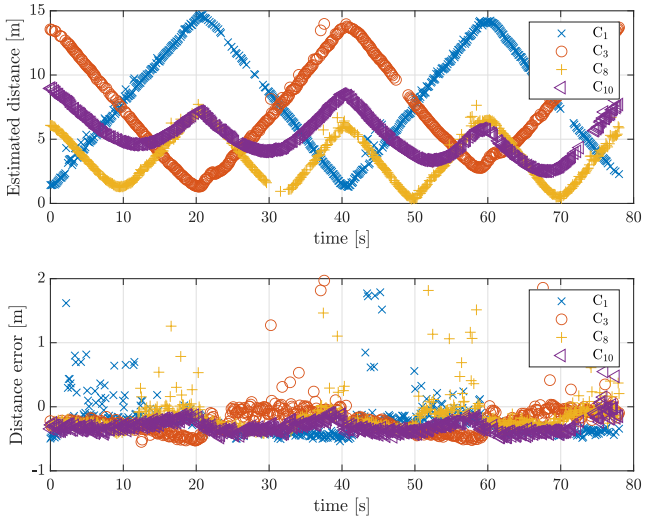

FIGURE 11 Estimated distance and distance error as a function of time in seconds for the mobile transceiving node and transceiving nodes C_1, C_3, C_8, and C_{10}.

performance for DFL, particularly, for time periods around 20 s, 40 s, and 60 s. During these time periods, the user moving at the edge or even outside the area spanned by the links in LoS, cf. Figure 10. Here, user-induced fading on the power can be measured for multiple MPCs, but only for very few links in LoS. That means, MDFL can compensate the lack of network links by considering MPCs, which eventually improves the localisation performance.

Figure 12 shows the CDFs of the localisation error for MDFL and DFL. We can observe that MDFL clearly outperforms DFL. With MDFL, we obtain in 80% of the cases an localisation error of less than 0.6 m whereas in case of DFL 4.4 m.

Figures 13 and 12 show additionally the RMSE and the CDF of the active localisation EKF. With a mean RMSE of 0.05 m, cf. Table 1, the active localisation EKF clearly outperforms the DFL and the MDFL. This is also visible in the CDF in Figure 12, where we can obtain a localisation error of less than 0.1 m in 80% of the cases. Nevertheless, the active localisation algorithm requires the user to carry a localisation device, that is, an actively transceiving node.

Note that for initialising an MDFL system, that is, for determining the propagation paths as well as for determining the parameters of the empirical exponential model, cf. Section 3, ground truth data of moving users are required. Given the high accuracy of the active localisation EKF, we can use this localisation solution for tracking users during an initialisation phase. Therewith, the UWB network may inherently provide a sufficient ground truth system for the initialisation of MDFL.

TABLE 1 Mean μ and standard deviation σ of the absolute positioning error.

	μ [m]	σ [m]
MDFL (PF)	0.40	0.53
DFL (PF)	2.52	1.38
Active loc. (EKF)	0.05	0.04

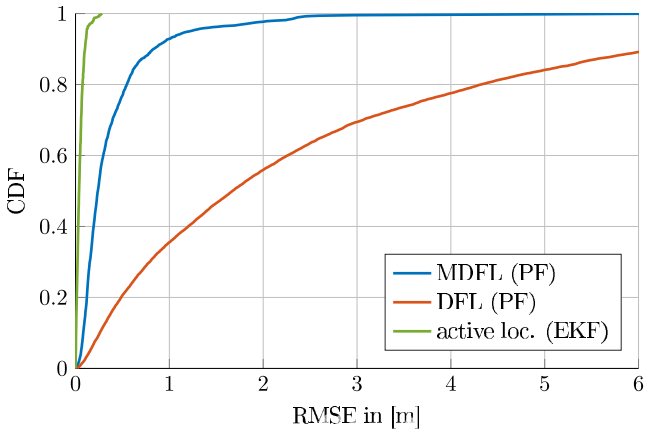

FIGURE 12 Cumulative distribution functions (CDFs) of the localisation error for MDFL (blue line) and DFL (red line), both realised by PFs, and active localisation algorithm realised by an EKF (green line).

5 | CONCLUSION

This work provides an overview of the required signal processing for multipath-enhanced device-free localisation (MDFL) using low-cost ultra-wideband (UWB) devices. We show how to access the channel impulse response of the Qorvo (DecaWave) *DW1000* module, how to estimate the required signal parameters, and introduce a Bayesian MDFL approach. Based on a meshed network of UWB devices, we demonstrate MDFL for an indoor scenario. We show, that MDFL can be realised using low-cost UWB devices. Given the fully-meshed network, MDFL clearly outperforms state-of-the-art device-free localisation in terms of accuracy and robustness. Additionally, we compare device-free localisation (DFL) and MDFL systems to an active localisation algorithm based on an extended Kalman filter (EKF). Obviously, the EKF outperforms the DFL and MDFL systems; however, shows the possibility of using an active transceiving node to initialise MDFL within the same system.

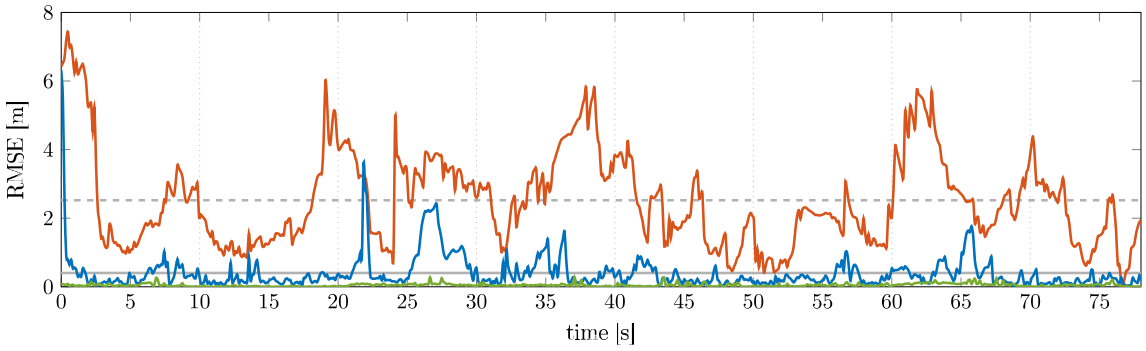

FIGURE 13 RMSE results over time for MDFL (blue line) and DFL (red line). Mean RMSE values for MDFL (0.40 m) and DFL (2.52 m) are indicated in grey, that is, as (grey line) and (doted grey line) respectively. Additionally, the RMSE results of the active localisation algorithm based on an EKF (green line) are given as reference.

AUTHOR CONTRIBUTIONS

Christian Gentner: Conceptualisation; Writing – Original Draft Preparation; Visualisation; Methodology; Software. **Martin Schmidhammer:** Conceptualisation; Writing – Original Draft Preparation; Visualisation; Methodology; Software.

ACKNOWLEDGEMENT

Open Access funding enabled and organized by Projekt DEAL.

CONFLICT OF INTEREST STATEMENT

The authors declare no conflicts of interest.

DATA AVAILABILITY STATEMENT

Research data are not shared.

ORCID

Christian Gentner https://orcid.org/0000-0003-4298-8195
Martin Schmidhammer https://orcid.org/0000-0002-9345-142X

REFERENCES

1. Gentner, C., et al.: Multipath assisted positioning with simultaneous localization and mapping. IEEE Trans. Wireless Commun. 15(9), 6104–6117 (2016). https://doi.org/10.1109/twc.2016.2578336
2. Patwari, N., Wilson, J.: RF sensor networks for device-free localization: measurements, models, and algorithms. Proc. IEEE 98(11), 1961–1973 (2010). https://doi.org/10.1109/jproc.2010.2052010
3. Schmidhammer, M., et al.: Multipath-enhanced device-free localization in wideband wireless networks. IEEE Antenn. Wireless Propag. Lett. 20(4), 453–457 (2021). https://doi.org/10.1109/lawp.2021.3052438
4. Guo, Y., et al.: An exponential-Rayleigh model for RSS-based device-free localization and tracking. IEEE Trans. Mobile Comput. 14(3), 484–494 (2015). https://doi.org/10.1109/tmc.2014.2329007
5. Lei, T., et al.: Enhanced geometric filtering method based device-free localization with UWB wireless network. IEEE Trans. Veh. Technol. 70(8), 7734–7748 (2021). https://doi.org/10.1109/tvt.2021.3090433
6. Kaltiokallio, O., Hostettler, R., Patwari, N.: A novel Bayesian filter for RSS-based device-free localization and tracking. IEEE Trans. Mobile Comput. 20(3), 780–795 (2021). https://doi.org/10.1109/tmc.2019.2953474
7. Schmidhammer, M., et al.: Bayesian multipath-enhanced device-free localisation: simulation- and measurement-based evaluation. IET Microw., Antennas Propag. 16(6), 327–337 (2022). https://doi.org/10.1049/mia2.12244
8. Schmidhammer, M., et al.: Bayesian approaches to multipath-enhanced device-free localization. In: 2021 15th European Conference on Antennas and Propagation (EuCAP 2021) (2021)
9. Schmidhammer, M., Gentner, C.: Multipath-enhanced device-free localization using low-cost ultra-wideband devices. In: 2022 16th European Conference on Antennas and Propagation (EuCAP 2021) (2022)
10. Decawave: DW1000 user manual - how to use, configure and program the DW1000 UWB transceiver version 2.18. User Man. (2017)
11. Schmidhammer, M., et al.: Distributed measurement framework for UWB communications, localization, and sensing. In: 2023 17th European Conference on Antennas and Propagation (EuCAP 2023) (2023)
12. Molisch, A.F.: Ultra-wide-band propagation channels. Proc. IEEE 97(2), 353–371 (2009). https://doi.org/10.1109/jproc.2008.2008836
13. Denis, B., Pierrot, J.B., Abou.Rjeily, C.: Joint distributed synchronization and positioning in uwb ad hoc networks using toa. IEEE Trans. Microw. Theor. Tech. 54(4), 1896–1911 (2006). https://doi.org/10.1109/tmtt.2006.872082
14. McElroy, C., Neirynck, D., McLaughlin, M.: Comparison of wireless clock synchronization algorithms for indoor location systems. In: 2014 IEEE International Conference on Communications Workshops (ICC), pp. 157–162 (2014)
15. Neirynck, D., Luk, E., McLaughlin, M.: An alternative double-sided two-way ranging method. In: 2016 13th Workshop on Positioning, Navigation and Communications (WPNC), pp. 1–4 (2016)
16. Fleury, B.H., et al.: Channel parameter estimation in mobile radio environments using the SAGE algorithm. IEEE J. Sel. Area. Commun. 17(3), 434–450 (1999). https://doi.org/10.1109/49.753729
17. Schuhmacher, D., Vo, B., Vo, B.: A consistent metric for performance evaluation of multi-object filters. IEEE Trans. Signal Process. 56(8), 3447–3457 (2008). https://doi.org/10.1109/tsp.2008.920469
18. Meissner, P., Leitinger, E., Witrisal, K.: UWB for robust indoor tracking: weighting of multipath components for efficient estimation. IEEE Wireless Commun. Lett. 3(5), 501–504 (2014). https://doi.org/10.1109/lwc.2014.2341636
19. Bar-Shalom, Y., Li, X., Kirubarajan, T.: Estimation with Applications to Tracking and Navigation: Theory, Algorithms and Software. John Wiley & Sons (2004)
20. Arulampalam, M.S., et al.: A tutorial on particle filters for online nonlinear/non-Gaussian Bayesian tracking. IEEE Trans. Signal Process. 50(2), 174–188 (2002). https://doi.org/10.1109/78.978374

How to cite this article: Gentner, C., Schmidhammer, M.: Ranging and multipath-enhanced device-free localisation with densely-meshed ultra-wideband devices. IET Microw. Antennas Propag. 17(8), 667–676 (2023). https://doi.org/10.1049/mia2.12373